New solutions to covariant nonequilibrium dynamics

Dénes Molnár and Miklos Gyulassy

Physics Department, Columbia University, 538 W. 120th Street, New York, New York 10027

New solutions of 3+1D covariant kinetic theory are presented for nuclear collisions in the energy domain $E_{c.m.} \sim 200A$ GeV. They are obtained using MPC, a new Monte Carlo parton transport technique that employs very high parton subdivision that is necessary to preserve covariance. The transport results are compared with ideal hydrodynamics solutions. We show that the transport evolution differs significantly from hydrodynamics. In addition, we compare the transport freeze-out distributions to those obtained from ideal hydrodynamics with the Cooper-Frye isotherm freeze-out prescription. The transport freeze-out four-volume is shown to be sensitive to the reaction rates and deviates from both timelike and spacelike freeze-out 3D hypersurfaces commonly assumed. In particular, we find that there does not exist a universal freeze-out temperature. Finally, the transverse momentum distributions are found to deviate by up to an order of magnitude from (Cooper-Frye frozen) hydrodynamics for a wide range of possible initial conditions and reaction rates at RHIC energies.

PACS number(s): 25.75.Ld, 24.10.Jv, 24.10.Lx

I. INTRODUCTION AND CONCLUSIONS

A theoretical framework to study nonequilibrium dynamics is provided by Boltzmann transport theory. The dynamical variables of this theory are the Lorentz-covariant, one-particle phase space distributions $f_i(x,p)$; while the dynamics is governed by transition probabilities $W_{c \to c'}$, which are Lorentz-covariant functions of the particle momenta. The theory, while not exact, is rather general. First, it is not restricted to particular particle types. The particles could be partons, hadrons, or molecules. Second, the reaction rates that specify the dynamics are also unrestricted in their origin. For example, the rates could emerge from an effective quantum field theory or Newtonian mechanics. The primary limitations of the theory are the neglect of dynamical correlations (one-body truncation of the formal BBGKY hierarchy [1]) and the inability, without additional classical fields, to model phase transition dynamics.

We consider here the simplest form of Lorentz-covariant Boltzmann transport theory in which the on-shell phase space density $f(x,\mathbf{p})$, evolves with an elastic $2 \to 2$ rate as [2–4]

$$p_1^\mu \partial_\mu f_1 = \int_2 \int_3 \int_4 (f_3 f_4 - f_1 f_2) W_{12 \to 34} \delta^4(p_1 + p_2 - p_3 - p_4)$$
$$+ S(x, \mathbf{p}_1). \qquad (1)$$

Here W is the square of the scattering matrix element, the integrals are shorthands for $\int_i \equiv \int [g \, d^3 p_i / (2\pi)^3 E_i]$, where g is the number of internal degrees of freedom, while $f_j \equiv f(x, \mathbf{p}_j)$. The initial conditions are specified by the source function $S(x, \mathbf{p})$, which we discuss later in Sec. II. For our applications below, we interpret $f(x,\mathbf{p})$ as describing an ultrarelativistic massless gluon gas with $g = 16$ (eight colors, two helicities).

Recall several important properties of Eq. (1). First, the particle number current and the energy-momentum tensor are given by

$$N^\mu(x) \equiv \int \frac{d^3 p}{(2\pi)^3 E} p^\mu f(x, \mathbf{p}) \qquad (2)$$

and

$$T^{\mu\nu}(x) \equiv \int \frac{d^3 p}{(2\pi)^3 E} p^\mu p^\nu f(x, \mathbf{p}). \qquad (3)$$

With these definitions, particle number and energy-momentum conservation *follow* from Eq. (1) [when the source term $S(x, \mathbf{p}) = 0$]. Second, there is a class of fixed points, called *global equilibria*, which are phase space densities of the form

$$f(x, \mathbf{p}) = \frac{g}{(2\pi)^3} \exp\left[\frac{\mu - p_\mu u^\mu}{T}\right], \qquad (4)$$

where u_μ is a constant four-vector that specifies a global flow velocity, while T and μ correspond to the constant temperature and chemical potential. Furthermore, the *H-theorem* [1] states that the Boltzmann transport equation drives the system towards global equilibrium.

Despite its relatively simple form, the Boltzmann equation is nonlinear with very few known analytic solutions. Until recently, progress to obtain even numerical solutions has been hampered by its numerical complexity. The rapid increase in computational power has finally made it possible to break through this barrier. For nuclear collision applications, new numerical algorithms are being developed, tested, and made available via the World Wide Web under a new Open Standard for Codes and Routines (OSCAR) [5]. The present work is a further step in that development.

For nuclear collisions at SPS energies ($\sqrt{s} \lesssim 20A$ GeV), numerical solutions of hadronic transport models have been available for some time [6]. However, for higher collider energies, the emergence of massless partonic degrees of freedom creates the technical challenge of how to retain Lorentz covariance. In this paper we present results based on a new

numerical technique, MPC 0.1.2 [4], that provides reliable solutions in this ultrarelativistic regime.

The difficulty of the analytic treatment of the Boltzmann transport equation has forced workers in the past to make strong simplifying assumptions. A common simplification has been to ignore the general nonequilibrium problem and to postulate that *local equilibrium* is maintained at all times. In the framework of the Boltzmann transport theory, this choice corresponds to substituting a local equilibrium ansatz in place of the fixed point global equilibria. Allowing (u_μ, T, μ) to vary with the coordinate x^μ, this ansatz corresponds to

$$f(x, \mathbf{p}) = \frac{g}{(2\pi)^3} \exp\left[\frac{\mu(x) - p_\mu u^\mu(x)}{T(x)} \right]. \quad (5)$$

It is however well known that local equilibrium is *not* a solution of Eq. (1). The nonlinear collision term vanishes in local equilibrium, but $p^\mu \partial_\mu f \neq 0$ in general. Only in the limit when all the rates go to infinity, i.e., when the mean free path goes to zero, can the solution approach local equilibrium.

A covariant, dynamical theory can nevertheless be postulated based on the assumption of local equilibrium. That is relativistic hydrodynamics [7], which is widely used in heavy-ion physics [8,9] to calculate observables. Assuming an equilibrium initial condition specified on a hypersurface $\sigma_{in}^\mu(x)$, the local energy momentum and baryon number conservation laws

$$\partial^\mu T_{\mu\nu} = 0, \quad \partial^\mu N_{B,\mu} = 0 \quad (6)$$

reduce to (Euler) hydrodynamical equations under the assumptions that local chemical and thermal equilibrium are maintained and that dissipation (viscosity and thermal conductivity) can be neglected. In that case, the energy-momentum tensor and baryon current can be expressed as $T_{\mu\nu} = u_\mu u_\nu (e + p) - g_{\mu\nu} p$ and $N_{B,\mu} = u_\mu n(x)$ in terms of the local flow velocity $u_\mu(x)$, local pressure $p(x)$, local energy density $e(x)$, and local proper density $n(x)$. The equations form a closed system if, in addition, the equation of state, $e(p, n_B)$, is specified.

It is clear that the idealization of local equilibrium may apply, if at all, only in the interior of the reaction volume, where the local mean free path $\lambda(x) = 1/(\sigma n(x))$ may remain small for a while as compared to the characteristic dimensions and gradients of the system, $L_\mu(x) \sim |\partial_\mu \log e(x)|^{-1}$. However, these assumptions are marginal for conditions encountered in heavy ion collisions and certainly break down near the surface region and throughout the freeze-out phase. Due to longitudinal expansion the density decreases as $1/\tau$ until $\tau \sim \sqrt{3}R$ when three-dimensional expansion rapidly increases λ beyond L.

For small departures from local equilibrium, corrections to the ideal Euler hydrodynamic evolution can be calculated by taking the $T^{\mu\nu}$ and N_B^μ moments of an underlying kinetic theory. To first order in λ/L, the equations reduce to the Navier-Stokes equations. The solutions to Navier-Stokes depend therefore not only on the equation of state, but also on the bulk and shear viscosity and thermal conductivity trans-

port coefficients of the medium. While such an approach has proven useful in nonrelativistic problems and in special relativistic geometries, severe problems of instability and acausality appear when extended into the ultrarelativistic domain [10].

The newly formulated, covariant, parton kinetic theory technique, MPC [4], allows us to compute the highly dissipative evolution during the densest partonic phase of the reaction in a covariant manner as well as investigate the final freeze-out dynamics. MPC is an extension of Zhang's covariant parton cascade algorithm, ZPC [3]. Both MPC and ZPC have been extensively tested [11,12] and compared to analytic transport solutions and covariant Euler and Navier-Stokes dynamics in 1+1D geometry. A critical new element of both these algorithms is the parton subdivision technique proposed by Pang [2,12]. As shown in detail in Sec. III, rather high subdivision ~ 100 is needed to preserve Lorentz covariance numerically for massless parton evolution.

Extensions of MPC to include inelastic $2 \leftrightarrow 3$ partonic processes [13] are under development, but in this paper we use MPC in the pure elastic parton interactions mode as in ZPC [5].

The aim of this work is to calculate the sensitivity of the evolution and freeze-out of an ultrarelativistic (massless) parton system to the transport rates and initial conditions expected in Au+Au reactions at RHIC energies ($\sqrt{s} \sim 200A$ GeV). We compare the results to the (OSCAR compliant) relativistic Euler hydrodynamic code developed by Rischke and Dumitru [5,14]. An ideal gas ($e = 3p$) equation of state is used in that analysis. This work extends Refs. [11,15], focusing on the freeze-out problem in (3+1)-dimensional Bjorken expansion. It is less ambitious than for example Ref. [15] by limiting the study to massless partons. This avoids introducing yet further complications due to dissipative hadronization and hadronic transport effects. The initial conditions are taken from the HIJING multiple minijet generator [5,16].

One of the main results of this work is shown in Fig. 1. To test whether ideal hydrodynamics is an adequate approximation of the parton transport equation (1), we have followed the evolution both for the Boltzmann equation (1) and Euler hydrodynamics from the *same* RHIC initial condition from [16]. (See Sec. V for details of the simulations.) Figure 1 shows the evolution of the transverse energy dE_t/dy at midrapidity. There is a large difference between the transport and hydrodynamic solutions in both the (1+1)- and (3+1)-dimensional case, even for a physically extreme, 15 mb, cross section. Note that these 15 mb curves are equivalent[1] to a solution for 3 mb cross section with five times higher [17] initial density than expected with HIJING. Therefore, large deviations from ideal hydrodynamics are to be expected for possible initial conditions at RHIC. In addition, this conclusion is independent of the initial system size (see explanation in Sec. V A).

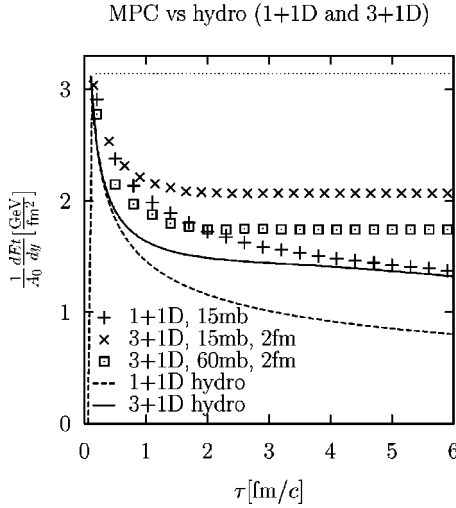[1] The equivalence is due to the scaling property of Eq. (1) explained in Sec. III.

FIG. 1. This figure shows the evolution of the transverse energy dE_t/dy at midrapidity, normalized by the initial transverse area, from kinetic theory and from hydrodynamics both for $1+1$ (transverse periodic) and $3+1$ dimensions. The initial distribution was a Bjorken cylinder with a radius $R_0 = 2$ fm at proper time $\tau_0 = 0.1$ fm/c in local thermal and chemical equilibrium at $T_0 = 500$ MeV. The cross sections were $\sigma = 15$ and 60 mb, with the cutoff $\mu = 0.5$ GeV. Note that the hydrodynamical results are *free from any arbitrary freeze-out prescription* because they depend only on the evolution of the phase space distribution ansatz (5) as dictated by the equations of motion (6). The difference between the hydrodynamical and the kinetic theory results, even for a large, 60 mb cross section, indicates that ideal hydrodynamics is not applicable for the evolution.

This conclusion reinforces the results of Ref. [11], where it was shown that large deviations even from the Navier-Stokes evolution in $(1+1)$D Bjorken expansion are expected for initial densities up to four times higher than predicted by the HIJING model [16].

A second main result of this work is shown in Fig. 2. We tested whether the widely used Cooper-Frye freeze-out prescription could ''correct'' final observables for the neglect of the early breakdown of ideal hydrodynamics. Figure 2 shows the final, experimentally observable $p_\perp$ distributions divided by the thermal initial distribution. We find that there is an order of magnitude difference between transport and hydrodynamic solutions at *both* low and at high $p_\perp$ for realistic ($\sim$ few mb) gluonic cross sections. The difference is still a factor of two to three even for a physically extreme, 15 mb, cross section. In addition, increasing the radius of the initial Bjorken cylinder from 2 to 6 fm does not reduce the discrepancy between the covariant transport solutions and those of Cooper-Frye frozen hydrodynamics. To get closer to the transport $p_\perp$ distributions, one would have to choose a freeze-out temperature much above the commonly assumed 100–150 MeV range.

The last main result of this work is illustrated in Fig. 3. This shows that high hydrodynamic freeze-out temperatures that would be needed to ''fit'' the transport solutions are, however, inconsistent with the space-time freeze-out distributions of covariant transport theory. Unlike the ''sharp''
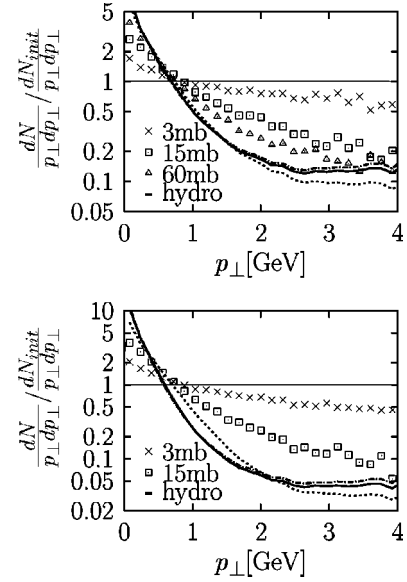

FIG. 2. The top figure shows the freeze-out $p_\perp$ distributions relative to the *initial* ($T_0 = 500$ MeV) $p_\perp$ distribution from an initial radius $R_0 = 2$ fm for the cascade with $\sigma = 3$, 15, 60 mb, and for ideal hydrodynamics with Cooper-Frye freeze-out with freeze-out temperatures $T_f = 100$ MeV (dashed-dotted line), 130 MeV (thick solid line), and 200 MeV (dotted line). The bottom figure shows the same but for an initial radius $R_0 = 6$ fm with cross sections 3 and 15 mb.

space-time freeze-out particle distributions commonly assumed using the Cooper-Frye freeze-out prescription, the transport theory freeze-out volume is four-dimensional. Particles freeze out over a large four-volume that forms a wedgelike freeze-out region in the $\tau - R$ plane. This freeze-out distribution depends strongly on the microscopic reaction rates (higher rates lead to a later freeze-out). It is *not* possible to tune the Cooper-Frye freeze-out temperature to reproduce the cascade freeze-out distributions. Though one can arrange that the Cooper-Frye freeze-out curve follows more-or-less the ridge, the transport distribution *along* that ridge is not correctly reproduced by Cooper-Frye frozen hydrodynamics. In particular, hydrodynamic freeze-out surfaces with a time-like section result in unphysical spikes in the $dN/d\tau$ distribution which are not present in the transport theory calculations. These spikes arise when the freeze-out temperature is such that the interior of the system freezes out due to longitudinal Bjorken expansion (see Sec. V B 1 for further discussion).

In summary, our results show that for a rather wide range of initial conditions at RHIC energies, the evolution of the system deviates strongly from Eulerian hydrodynamics throughout the $(3+1)$D evolution. It is not possible to mimic the observables from the nonequilibrium evolution by simply applying the isotherm Cooper-Frye freeze-out prescription to ideal hydrodynamics. The space-time four-volume of freeze-out, even for the largest ($R \sim 6$ fm) nuclei, does not resemble a timelike surface. In addition, the observable transverse momentum spectra are very sensitive to the microscopic reaction rates. These results indicate that while ideal hydrodynamics is a useful model to explore possible collective
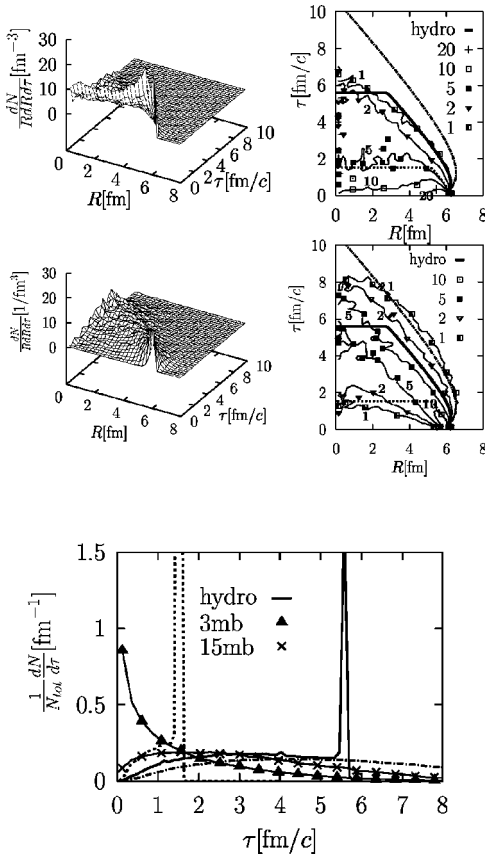
FIG. 3. The left column shows the transverse coordinate and proper time distribution $dN/RdRd\tau$, of freeze-out coordinates. Top row corresponds to $\sigma=3$ mb and middle row to 15 mb. The initial Bjorken cylinder radius is $R_0=6$ fm in both cases. The right column shows contour plots corresponding to the left column. The thick lines show Cooper-Frye isotherms: $T_f=100$ MeV (dashed-dotted line), 130 MeV (thick solid line), and 200 MeV (dotted line). The bottom figure compares the proper time freeze-out distribution, $dN/d\tau$, for the different cases.

dynamics in nuclear collisions, the interpretation of experimental observables must take into account the finite transition probabilities $W_{\{i\}\to\{j\}}$ that govern the nonequilibrium evolution. Fortunately, numerical techniques such as MPC and ZPC are now readily available [5]. Experimentally, the A, $E_{c.m.}$, and multiplicity dependence of the observables provides the best way to measure these effective reaction rates in the ultradense matter formed in nuclear collisions.

II. COVARIANT PARTON TRANSPORT THEORY

Equation (1) is the simplest form of classical Lorentz-covariant Boltzmann transport theory. In principle, the transport equation could be extended for bosons with the substitution $f_1 f_2 \to f_1 f_2 (1+f_3)(1+f_4)$ and a similar one for $f_3 f_4$ [where we used the short-hand $f_i \equiv f(x,\mathbf{p}_i)$]. In practice, no covariant algorithm yet exists to handle such nonlinearities. We therefore limit our study to quadratic dependence of the collision integral on f.

The elastic gluon scattering matrix elements in dense parton systems are typically of the Debye-screened form:

$d\sigma/dq^2 \approx (9\pi\alpha_s^2/2)/(q^2+\mu^2)^2$, which favors small angle scattering [11]. However, the relevant transport cross section is $\sigma_t = \int d\sigma \sin^2\theta_{c.m.} \approx (9\pi\alpha^2/2s)\log(s/4\mu^2)$, where $s \approx 17T^2$. In order to maximize the equilibration rate for a fixed cross section, we take here an *isotropic* differential cross section in the center-of-mass frame instead. We further assume an energy-independent cross section with a threshold specified by μ^2, i.e., our solutions therefore correspond to the microscopic dynamics specified by the following idealized model:

$$d\sigma = \Theta(s^2-\mu^2)\frac{\sigma_0}{4\pi}d\Omega. \qquad (7)$$

The transport cross section is $2\sigma_0/3$ in this case.

It is important to emphasize that while the cross section suggests a geometrical picture of action over finite distances, we use Eq. (7) only as a convenient parametrization to describe the effective *local* transition probability, W. In the present study this is simply modeled as $dW/d\Omega = s d\sigma/d\Omega$. The particle subdivision technique (see next section) needed to recover covariance removes all notion of nonlocality in this approach, just like in hydrodynamics. Thus, the cross sections, e.g., 60 mb, used in the present study to simulate rapid local changes of the phase space density in no way imply that distances bigger than 1 fm play any role.

With the above cutoff μ, freeze-out of a test particle can arise in two different ways: either the system becomes too *dilute*, i.e., $1/n\sigma_0 \gg L$, or the system *cools* down and the threshold suppresses further interactions. By construction, the possibility for the latter case occurs along an isotherm, $T_f \approx \mu/\sqrt{17}$. With Eq. (7), we can therefore study the influence of dissipative phenomena by varying the two scales σ_0 and μ^2. The evolution was performed with $\sigma_0=3, 15, 30, 60, 121$ mb and $\mu=0, 0.1, 0.5$ GeV.

The initial condition was taken to be a longitudinally boost invariant Bjorken cylinder in local thermal and chemical equilibrium at temperature $T(\tau_0)=500$ MeV at proper time $\tau_0=0.1$ fm/c as by fitting the gluon mini-jet transverse momentum spectrum predicted by HIJING [16]. In order to compare to hydrodynamics, we assume that the transverse density distribution is uniform up to a radius $R_0=2, 4, 6$, or 8 fm. The pseudorapidity $\eta \equiv 1/2\log[(t+z)/(t-z)]$ distribution was taken as uniform between $|\eta|<5$. Since we want to compare to chemically and thermally equilibrated hydrodynamics,[2] the equilibrium initial gluon density was taken for this $T(\tau_0)$ to be

$$n_{\eta,0} \equiv \frac{dN}{d\eta d^2 x_\perp}\bigg|_{\tau_0} = \frac{g}{\pi^2}T^3\tau_0 \approx 2.65 \text{ fm}^{-2}. \qquad (8)$$

---

[2]Technically, MPC was run with an out-of-chemical-equilibrium initial gluon density $n_{\eta,0}=4$ fm^{-2} as obtained via HIJING including final state radiation and with cross sections $\sigma_0=2, 10, 20, 40$, and 80 mb. As explained in Sec. III, because of the scaling property of the solutions of the transport equation, the solutions for the chemical equilibrium initial condition are identical when the cross section is rescaled by a factor $l=2.6505/4 \approx 1/1.509$.

Evolutions from different initial densities can be obtained by varying the cross section only and using the scaling property explained in the next section.

III. PARTON SUBDIVISION AND SCALING OF SOLUTIONS

We utilize the parton cascade method to solve the Boltzmann transport equation (1). A critical drawback of all cascade algorithms is that they inevitably lead to numerical artifacts because they violate Lorentz covariance. This occurs because particle interactions are assumed to occur whenever the distance of closest approach (in the relative c.m.) is $d < \sqrt{\sigma_0/\pi}$, which corresponds to action at a distance. To recover the *local* character of equation (1) and hence Lorentz covariance, it is essential to use the parton subdivision technique [2,3]. This is based on the covariance of Eq. (1) under the transformation

$$f \to f' \equiv lf, \quad W \to W' \equiv W/l \quad (\sigma \to \sigma' = \sigma/l). \quad (9)$$

As shown in Ref. [12], the magnitude of numerical artifacts is governed by the diluteness of the system $\sqrt{\sigma}/\lambda_{\mathrm{MFP}}$, that scales with $1/\sqrt{l}$. Lorentz violation therefore formally vanishes in the $l \to \infty$ limit.

A. Convergence with subdivision

Figure 4 illustrates the severeness of the cascade numerical artifacts in the case of insufficient particle subdivision. The top plot in Fig. 4 shows that the parton cascade solution for the evolution of the transverse energy per unit rapidity does not converge until the subdivision factor reaches $l \sim 100$. The lack of covariance can be seen in the difference between the solutions in frames separated by 3 units of rapidity. The very fact that the cascade evolution is different for different particle subdivisions means that the subdivision covariance (9) is itself violated by the cascade algorithm. Nevertheless, both Lorentz and subdivision covariance are recovered when l is sufficiently large.

The large overshoot in the dE_t/dy evolution is a result of the superluminal signal propagation speed inherent to the cascade algorithm. A cascade particle can influence almost *instantaneously* another cascade particle that is within the interaction range $r_\sigma \equiv \sqrt{\sigma/\pi}$. In a very dense system, a ''chain'' of almost instantaneous interactions can occur causing long range superluminal artifacts.

As a measure of the signal propagation speed in a nonlocal collision in the cascade we define

$$\mathbf{v}_s \equiv \frac{\mathbf{x}_{\mathrm{partner}}(t_{\mathrm{collision}}) - \mathbf{x}_{\mathrm{particle}}(t_{\mathrm{last\ collision}})}{t_{\mathrm{collision}} - t_{\mathrm{last\ collision}}}. \quad (10)$$

Analytically, the deviation of the signal propagation speed from the speed up light can be roughly approximated by
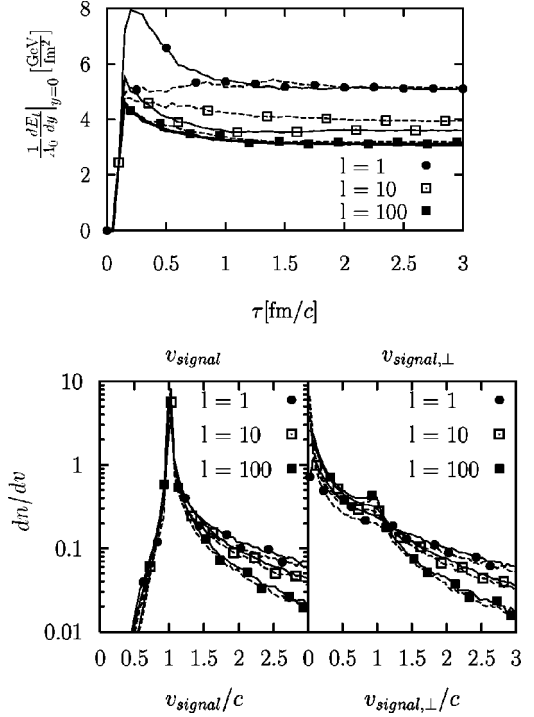
$$\Delta v_s = \frac{r}{t}, \quad (11)$$

FIG. 4. The top figure shows the E_t evolution at midrapidity (solid lines) for subdivision factors $l=1$, 10, 100 from the initial condition $R_0=2$ fm, $\sigma=10$ mb, $n_{\eta,0}=4$ fm^{-2}, $T_0=\mu=0.5$ GeV, $\tau_0=0.1$ fm/c. The dashed curves are for the same initial condition but all particles were boosted longitudinally by 3 units of rapidity and dE_t/dy was computed at $y=3$. Though not visible, the curve for $l=400$ falls on top of the $l=100$ curve. The bottom plots show the normalized distribution of the signal propagation velocity averaged over the full evolution.

where t is the time between the collision and the previous collision, while r is the distance between the colliding particles at the time of the collision ($r < r_\sigma$). This is a pessimistic estimate that maximizes the deviations. Assuming that subsequent collisions are uncorrelated, t follows a Poisson distribution[3]

$$P(t) \equiv \frac{dn}{dt} = \frac{1}{\lambda} \exp(-t/\lambda). \quad (12)$$

Hence the distribution of Δv_s (with r fixed) is

$$P(\Delta v_s) = \frac{dn}{dt} \frac{dt}{d\Delta v_s} = \frac{r}{(\Delta v_s)^2 \lambda} \exp\left(-\frac{r}{|\Delta v_s|\lambda}\right). \quad (13)$$

Particle subdivision reduces r_σ as $r_\sigma(l) = r_\sigma(1)/\sqrt{l}$. Therefore, in the large subdivision limit, the subluminal and superluminal tails of the signal velocity distribution scale as a power law

$$P(\Delta v_s) \sim \left(\frac{v_0/\sqrt[4]{l}}{\Delta v_s}\right)^2, \quad v_0 \equiv \sqrt{\frac{r}{\lambda}}, \quad (14)$$

---

[3] The scaling (9) leaves the mean free path λ invariant.

i.e., the distribution gets narrower as $P_l(\Delta v_s) \sim P_1(\Delta v_s \sqrt[4]{l})$.

The ''measured'' cascade distributions of the magnitude of the signal propagation speed, dn/dv_s, as defined via Eq. (10), and the magnitude of its transverse component, $dn/dv_{s,\perp}$, are shown in Fig. 4. Though the distribution of v_s is strongly peaked at $v_s = c$, both super- and subluminal propagation are present. While increasing particle subdivision decreases the deviations from the exact propagation speed c, convergence is slow. Even for a subdivision of 100, 13% of the collisions correspond to a signal propagation velocity larger than $1.5c$. One must keep in mind that Fig. 4 shows the distribution of the signal propagation speed measured over the length and time scale of a single collision. On larger scales, the deviation is reduced because the large scale signal velocity is the sum of many small scale signal velocities.

In summary we demonstrated that the numerical artifacts due to Lorentz violation and acausality are reduced by subdivision and the cascade solution converges as l increases. In the $l \to \infty$ limit the cascade technique gives the correct numerical solution of the transport equation (1). In practice, rather high subdivisions were found necessary to recover covariance. We could explore convergence up to $l = 800$, 200, 150, and 100, for $R_0 = 2$, 4, 6, and 8 fm with the workstations available to us.

B. Scaling of the transport solutions

Subdivision covariance (9) actually implies that the transport equation has a broad dynamical range, and the solution for any given initial condition and transport property immediately provides the solution to a broad band of suitably scaled initial conditions and transport properties. This is because solutions for problems with l times larger the initial density $dN/d\eta d^2 x_\perp$, but with one lth the reaction rate can be mapped to the original ($l=1$) case for *any* l. We must use subdivision to eliminate numerical artifacts. However, once that is achieved, we have actually found the solution to a whole class of suitably rescaled problems.

The dynamical range of the transport equation (1) is further increased by its covariance under coordinate rescaling

$$f(x,\mathbf{p}) \to f'(x,\mathbf{p}) \equiv f\left(\frac{x}{l_x}, \mathbf{p}\right), \qquad W \to W' \equiv \frac{W}{l_x}. \quad (15)$$

This is a simultaneous rescaling of space-time *and* the transition probability. In addition, there is also a covariance under rescaling of the momenta

$$f(x,\mathbf{p}) \to f'(x,\mathbf{p}) \equiv l_p^{-3} f\left(x, \frac{\mathbf{p}}{l_p}\right),$$

$$W(\{p_i\}) \to W'(\{p_i\}) \equiv l_p^2 W\left(\left\{\frac{p_i}{l_p}\right\}\right), \quad (16)$$

such that the particle density is again unchanged. This scaling also implies a rescaling of the mass $m \to m' = m/l_p$. Combining the three scaling transformations, we find covariance of the transport theory under

TABLE I. Solutions for the sets of parameters below were computed via MPC for the present study.

μ/T_0	R_0/τ_0	$\sigma n_{\eta,0}$	μ/T_0	R_0/τ_0	$\sigma n_{\eta,0}$	μ/T_0	R_0/τ_0	$\sigma n_{\eta,0}$
0	20	4	1	6	4	1	40	8
0	40	4	1	8	4	1	40	16
0.2	20	4	1	20	0.8	1	60	0.8
0.2	40	4	1	20	4	1	60	4
1	2	0.8	1	20	8	1	80	0.8
1	2	4	1	20	16	1	80	4
1	2	16	1	40	0.8			
1	4	4	1	40	4			

$$f(x,\mathbf{p}) \to f'(x,\mathbf{p}) \equiv l_p^{-3} l f\left(\frac{x}{l_x}, \frac{\mathbf{p}}{l_p}\right),$$

$$W(\{p_i\}) \to W'(\{p_i\}) \equiv \frac{l_p^2}{l_x l} W\left(\left\{\frac{p_i}{l_p}\right\}\right). \quad (17)$$

In our calculation using MPC, we vary the physical parameters: σ, μ, T_0, R_0, τ_0, and $n_{\eta,0} \equiv dN/d\eta d^2 x_\perp|_{\tau_0}$ (the rapidity interval $\eta_{max} = 5$ was fixed). Keeping in mind Eq. (A3) and that

$$n_\eta \equiv \left. \frac{dN}{dy d^2_{x_\perp}} \right|_\tau = \int d^2 p_\perp\, d\eta\, m_t \mathrm{ch}(y - \eta)\, \tau f(\mathbf{x}_\perp, \eta, \tau, \mathbf{p}_\perp, y),$$

covariance under the transformation (17) implies that once the solution for a particular choice of these parameters is known, then the solution is known for any other choice of the parameters which are related to the original via

$$\sigma' = l_x^{-1} l^{-1} \sigma, \quad T_0' = l_p T_0, \quad R_0' = l_x R_0,$$

$$n_{\eta,0}' = l_x l n_{\eta,0}, \quad \mu' = l_p \mu, \quad \tau_0' = l_x \tau_0. \quad (18)$$

Therefore, we can scale one solution to others provided that μ/T_0, R_0/τ_0, and $\sigma n_{\eta,0} \sim \tau_0/\bar{\lambda}_{\mathrm{MFP}}$ remain the same. For example, three times the density with one-third the cross section leaves all three parameters the same, hence the results can be obtained via scaling without further computation. Table I shows sets of the three ratios that we mapped out via MPC.

IV. FREEZE-OUT

A. Hydrodynamic freeze-out problem

In Sec. I we argued that hydrodynamics cannot be valid during the complete evolution in nuclear collisions because the assumption of local equilibrium breaks down. Thus, in

spite of its appeal, hydrodynamics cannot be compared with measurements without *additional* model assumptions needed to specify when and how it breaks down. The problem of determining those extra model assumptions is the so-called freeze-out problem.

For application to nuclear collisions, freeze-out cannot be formulated as an expansion in λ/L since by definition it occurs when that ratio exceeds unity. Hence, even the Navier-Stokes hydrodynamics is inadequate to solve the freeze-out problem.

A common freeze-out prescription, which we here name ''Cooper-Frye frozen hydrodynamics,'' is to assume the validity of ideal hydrodynamics up to a ''sharp'' 3D freeze-out hypersurface $\sigma^\mu(x)$. Assuming that all interactions suddenly cease on that hypersurface, the final (frozen-out) invariant differential distribution of particles is then computed via the Cooper-Frye formula [18]:

$$EdN = \frac{d^3p}{(2\pi)^3} d\sigma^\mu(x) p_\mu f(x,\mathbf{p}). \qquad (19)$$

Here $d\sigma^\mu(\mathrm{x})$ is the normal vector to the 3D freeze-out hypersurface at the point x, while $f(x,\mathbf{p})$ is assumed to be in local equilibrium and hence, for classical particles, given by Eq. (5). While this prescription is covariant and appealingly simple, it suffers from several well known problems [9,19].

First, because the hydrodynamical solutions do not contain dynamical information needed to compute the freeze-out hypersurface, the assumed one is simply an *ad hoc* external constraint. It is usually parametrized in terms of a few physically ''reasonable'' parameters, the most common being a freeze-out isotherm $T(\sigma^\mu) = T_f$ or freeze-out energy density e_f. It is not possible to estimate the errors introduced by such a prescription.

Second, the Cooper-Frye formula allows negative contributions to the measurable particle yields [20–22]. This can be avoided [21–23] by choosing a nonequilibrium post freeze-out distribution that does not have particles in the phase space domain where $d\sigma^\mu p_\mu < 0$. However, such a choice still relies on the existence of a sharp 3D freeze-out surface.

Finally, while an idealized sharp freeze-out surface may be adequate for applications to quasistationary macroscopic systems, it cannot be justified in expanding mesoscopic systems in which L/λ is never large. The very fact that such systems do freeze out, i.e., $\lambda(\sigma) > L$, means that the solution to freeze-out problem must entail *global* information as the system becomes more and more dilute. Furthermore, there is no way to justify the neglect of final state interactions during freeze-out stage of the reactions while expansion and rarefaction are causing the system to depart from local equilibrium.

In Ref. [24] a continuous emission hydrodynamical freeze-out model was proposed to overcome some of these problems. The global information relevant to freeze-out in that model is taken there as the Glauber escape probability

$$P(x,p) = \exp\left(-\int_\tau^{\tau_{\mathrm{out}}} d\tau' \, \sigma v_{\mathrm{rel}} n(x(\tau))\right). \qquad (20)$$

This formula reveals clearly the highly nonlocal character of the freeze-out problem. At any point in space-time, x^μ, the line integral runs over the future trajectory and therefore is exponentially sensitive to the future evolution of the system. This leads to a formidable self-consistency problem. For special geometries such as Bjorken boost invariant expansion, a rough estimate of P can be made using the approximate scaling Bjorken hydrodynamic solution

$$n(x(\tau)) = \frac{\tau_0}{\tau} n(x(\tau_0)) \Theta[R^2 - (\mathbf{x}_\perp + \mathbf{v}_\perp \tau)^2]. \qquad (21)$$

Together with the Glauber straight line trajectory, this leads to the characteristic power law survival probability

$$P \sim \left(\frac{\tau}{\tau_{\mathrm{out}}}\right)^{\sigma\tau_0 n(\tau_0)}, \qquad (22)$$

that also appears, e.g., in the J/ψ suppression problem [25]. While Eq. (20) captures essential global physics of freeze-out, it is not complete since before freeze-out the trajectories cannot be straight if local equilibrium is maintained via the assumed hydrodynamic equations. Also, in the surface region where $P \sim 1/2$ neither hydrodynamics nor eikonal dynamics applies.

The solution to the freeze-out problem in classical mechanics is given by microscopic transport theory. A hybrid approach that partially reaches that end was proposed in Ref. [26], which combines partonic hydrodynamics with hadronic transport theory. In that approach, hydrodynamics is assumed to hold up to only some *intermediate* critical temperature hypersurface, $T(\sigma_{\mathrm{int}}^\mu) = T_c > T_f$, on which the fluid is converted to hadrons via the Cooper-Frye formula. Subsequent evolution of the hadronic system is then calculated by solving the hadronic transport theory as encoded in UrQMD. As noted in Ref. [24], the freeze-out surface is actually a diffuse four-volume, and in addition different hadronic species freeze out over different four-volume domains. This sequential freeze-out leads to strong observable correlations such as the mass dependence of final transverse spectra. The main limitation (and/or advantage) of the above hybrid model [27] is the need to assume the validity of hydrodynamics in the dense partonic phase of the collision. It is advantageous in that possible collective effects due to the quark-gluon confinement transition can be explored with hydrodynamics using ''realistic'' equations of state. It is disadvantageous in that it is far from clear that local equilibrium is ever reached during the evolution. Recall [11] that dissipative effects on even global observables such as the transverse energy per unit rapidity cannot be accurately calculated using the Navier-Stokes equations.

Despite these known complications of the freeze-out problem, ideal hydrodynamics and Cooper-Frye freeze-out are still commonly used to fit experimental data using isotherm freeze-out hypersurfaces and draw inferences about the underlying dynamics. The consistency and significance of interpretations based on such fits can only be assessed by comparing detailed dynamical transport calculations to the hydrodynamic limit (see Sec. V).

B. Formal definition for freeze-out

An important experimental observable aspect of the space-time evolution of kinetic theory is the freeze-out distribution. In the framework of discrete parton cascade dynamics, the definition of the freeze-out distribution, dN_{fo}, is the number of partons per $d^4x d^4p$ invariant phase space volume with momentum p^μ that have a collision at x^μ but suffer no more collisions. Given the trajectories $[\mathbf{x}_a(t), \mathbf{p}_a(t)]$ or the world lines $x_a^\mu(\tau)$ of all partons a, that distribution is given by the ensemble average of the space-time coordinates, $x_{af}^\mu \equiv [t_{af}, \mathbf{x}_a(t_{af})]$, of the *last* collision together with the final outgoing momentum, $\mathbf{p}(t_{af}+0^+)$:

$$f_{fo}(x,p) \equiv \frac{dN_{fo}}{d^4x d^4p}$$

$$= \left\langle \sum_a \delta(t-t_{af})\delta^3(\mathbf{x}-\mathbf{x}_a(t_{af})) \right.$$

$$\left. \times \delta^4(p-p_a(t_{af}+0^+)) \right\rangle. \qquad (23)$$

Because the freeze-out times, t_{af}, are distributed over a broad time interval, f_{fo} does *not* correspond to

$$f(x,p) = N \left\langle \int d\tau \delta^4(x-x(\tau))\delta^4(p-p(\tau)) \right\rangle \qquad (24)$$

at any time or on any fixed 3D hypersurface. Note that f measures the phase space density of the world lines $x^\mu(\tau)$ and their four-velocities at a single point x^μ. On the other hand, f_{fo} measures the phase space density of last scattering events, where the momentum p of a particle was last changed. Pion interferometry [28] measures the Fourier transform of f_{fo}. Note that even after integrating over the freeze-out points, the final observed momentum spectrum, $\int d^4x f_{fo}(x,p)$, is only equal to the Cooper-Frye formula if x_{af}^μ happen to lie on a sharp 3D hypersurface, $\sigma^\mu(\zeta_1,\zeta_2,\zeta_3)$. We can write the Cooper-Frye freeze-out distribution then as

$$\frac{dN_{CF}}{d^4x d^4p} = N \int d^3\zeta \delta^4(x-\sigma(\zeta))\delta^4(p-p(\sigma(\zeta))). \qquad (25)$$

As discussed in the Appendix, we can write the (on-shell) freeze-out distribution in terms of the solution of the Boltzmann equation as

$$E_1 \frac{dF_{fo}(x,\mathbf{p}_1)}{d^4x d^3p_1} \equiv P_0(x,\mathbf{p}_1) \times \left[S(x,\mathbf{p}_1) \right.$$

$$+ \int_3 \int_4 \int_5 W_{34\rightarrow 15}\delta^4(p_3+p_4-p_1$$

$$\left. -p_5)f_3 f_4 \right]. \qquad (26)$$

While neither normalized nor unique, this expression provides at least a *formal* definition of the freeze-out distribution

for the Boltzmann equation solely in terms of the phase space distribution $f(x,\mathbf{p})$, and the assumed transition probabilities $W_{ij\rightarrow kl}$.

V. NUMERICAL RESULTS

A. Kinetic versus hydrodynamic evolution

To test the ideal hydrodynamical assumptions against transport theory, it is essential to eliminate as many model differences as possible. For example, both the hydrodynamic model and the kinetic theory should have the same degrees of freedom, the same equation of state, and the same initial conditions. Equation (1) describes a gas that in thermal equilibrium has the equation of state $e=3p$, if the partons are massless. We therefore used this ideal gas equation of state in the hydrodynamical simulations. We also chose the transport initial condition to be in local equilibrium, since hydrodynamics is limited to such initial conditions.

The hydrodynamic algorithm used [14] is furthermore designed for particles without a conserved charge, i.e., the particle number changes as dictated by chemical equilibrium. The algorithm solves the energy-momentum conservation equation to obtain the energy density, pressure and flow evolution. Then, instead of the charge conservation equation, it exploits the relation between density, particle mass, and temperature in chemical equilibrium to compute the freeze-out particle distribution. It is important to note therefore that Eq. (1) with *elastic* collisions has the same hydrodynamic limit as the hydrodynamic model only if the partons are massless. This is because ideal hydrodynamics conserves entropy [29] and for massless particles in thermal and chemical equilibrium entropy conservation is equivalent to particle number conservation.[4] For massive particles, we would have to compare transport to hydrodynamics with particle conservation. Conversely, we would need to supplement Eq. (1) to include inelastic channels, such as $2\leftrightarrow 3$ in Ref. [13], to compare to chemically equilibrated hydrodynamics. In the infinite rate limit we recover the hydrodynamic model even though we have a fixed number of particles. However, when the solution is out of equilibrium (either thermal, chemical, or both), it does make a difference whether we include particle number changing processes or not.

To test whether ideal hydrodynamics is an adequate description of the parton transport theory (1), we compare the evolution of the transverse energy dE_t/dy at midrapidity from the two models. This comparison is free from any hydrodynamic freeze-out prescription because the transverse energy is given directly by the phase space distribution as

$$\left. \frac{dE_t}{dy} \right|_\tau = \tau \int d^2p_\perp d\eta d^2x_\perp m_t \cosh(y-\eta)$$

$$\times m_t f(y,\mathbf{p}_\perp,\eta,\mathbf{x}_\perp,\tau), \qquad (27)$$

where, through the local equilibrium ansatz (5), the hydrodynamic phase space evolution is determined by the evolution of the flow velocity and local temperature as dictated by the equations of motion (6).

Figure 1 shows the transverse energy evolution from transport theory and hydrodynamics, for an initial Bjorken

---

[4]Because in this case $s=4n$.

cylinder radius of 2 fm, with $\tau_0 = 0.1$ fm/c, $T_0 = \mu = 0.5$ GeV, $n_{\eta,0} = 2.6505$ fm^{-2} (via scaling), $\sigma = 15$, and 60 mb. [We chose $\eta_m = 5$, subdivisions 800 for $(3+1)$D, 256 for $(1+1)$D, and a 100 fm^2 transverse area for the $(1+1)$D evolution.]

The transverse energy decreases much faster from ideal hydrodynamics than from kinetic theory, both in $(1+1)$D and $(3+1)$D, showing that hydrodynamics does more work than the cascade. This is due to the different phase space evolution in the two models. The early discrepancy, even for cross sections as extreme as 15 or 60 mb, indicates that either the transport evolution gets very quickly out of equilibrium, or the *initial* evolution is close to equilibrium but the energy-momentum tensor is not ideal. Note that even if the latter is true, it does not necessarily mean that this initial, locally equilibrated, nonideal dynamics can be described by the Navier-Stokes equations.

The above conclusion holds for any initial system size larger than 2 fm as well. Since the $(1+1)$D curves correspond to the infinite transverse size limit, the hydrodynamic and transport evolutions for initial sizes larger than 2 fm will lie between the 2 fm and the $(1+1)$D curves for hydrodynamics and for transport theory, respectively. Because these two regions do not overlap, the discrepancy between ideal hydrodynamics and transport theory will not disappear with increasing system size.

B. Kinetic vs hydrodynamic freeze-out results

In the previous subsection we showed that parton kinetic theory does not reduce to ideal hydrodynamics for initial conditions at RHIC. Thus, the final observables from the two models can be similar *only if* the hydrodynamic freeze-out prescription helps mimic the observables from the nonequilibrium transport evolution.

Here we test whether one can reproduce the transport observables by a suitable choice of the hydrodynamic freeze-out parameters. We chose the widely-used Cooper-Frye freeze-out prescription (19) with isotherm freeze-out surfaces, despite all known problems discussed in Sec. IV. Hence, our only adjustable parameter is the freeze-out temperature. Since Eq. (1) describes Boltzmann classical particles, we must use the classical distribution (5) in the Cooper-Frye formula.

1. Coordinate space evolution

Freeze-out distributions in space-time from MPC are shown in Figs. 3 and 5. Due to the assumed cylindrical symmetry and longitudinal boost invariance, that distribution is only a function of τ and R.

Figures 3 and 5 show the freeze-out distribution for initial radii 6 fm and 2 fm, respectively, with $\tau_0 = 0.1$ fm/c, $T_0 = \mu = 0.5$ GeV, $n_{\eta,0} = 2.6505$ fm^{-2} (via scaling), $\sigma = 3$, 15, and 60 mb. For comparison, three different freeze-out isotherms are also shown from solution of Cooper-Frye frozen ideal hydrodynamics. (We chose $\eta_m = 5$, subdivisions 800 for 2 fm, and 150 for 6 fm.)

Unlike the sharp hydrodynamic freeze-out surface, the freeze-out distribution from the cascade is a broad *wedge*.
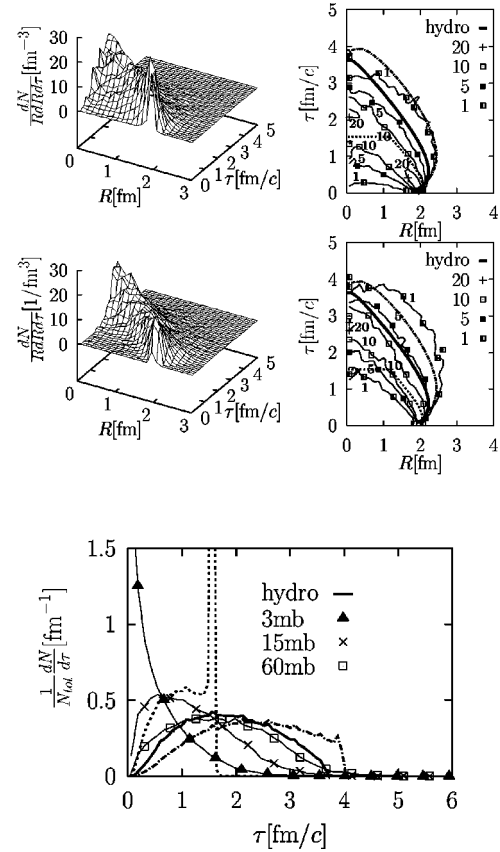

FIG. 5. The left column shows the transverse coordinate and proper time distribution, $dN/RdRd\tau$, of freeze-out coordinates. Top row corresponds to $\sigma = 15$ mb and middle row to 60 mb. The initial Bjorken cylinder radius is $R_0 = 2$ fm in both cases in contrast to Fig. 3, where $R_0 = 6$ fm. The right column shows contour plots corresponding to the left column. The thick lines show Cooper-Frye isotherms: $T_f = 100$ MeV (dashed-dotted line), 130 MeV (thick solid line), and 200 MeV (dotted line). The bottom figure compares the proper time freeze-out distribution, $dN/d\tau$, for the different cases.

Particles originate from a hypervolume in space-time, rather than from a hypersurface. In the top left plot (3 mb, 6 fm) in Fig. 3, the wedge moved down to $\tau = \tau_0$, which is a general feature for very low reaction rates. In the limit of a vanishing reaction rate, all particles freeze out from $\tau = \tau_0$.

Figures 3 and 5 show that particles freeze out later with increasing microscopic rates as expected. The maximum of the wedge moves outward with increasing rates, hence no freeze-out temperature can be universal. If we tune the freeze-out temperature to get as close as possible to the cascade freeze-out distribution, the freeze-out temperature will depend on the reaction rate.

Thus, the remarkable agreement seen in the bottom figure of Fig. 5 between Cooper-Frye frozen ideal hydrodynamics with a 130 MeV freeze-out temperature and the cascade with $\sigma = 60$ mb is a mere coincidence; higher rates would lead to a later freeze-out. For very high reaction rates, the 130-MeV hypersurface *from the cascade* would be very close to that from hydrodynamics because the hydrodynamic evolution is the infinite reaction rate limit of the cascade evolution. But

that does not mean that the freeze-out distributions are the same. On the contrary, if hydrodynamics and the cascade are close to each other at $T = 130$ MeV then we have no justification to stop the hydrodynamic evolution and freeze out with Eq. (19) because we are still in equilibrium and particles will certainly collide in the future, i.e., they have not yet frozen out.

It is *not* possible to tune the Cooper-Frye freeze-out temperature to reproduce the cascade freeze-out distribution. Though the contour plots in Figs. 3 and 5 suggest that such a tuning can get the hydrodynamic freeze-out *curve* close to the *ridge of the wedge* of the cascade freeze-out distribution, that is not enough. As the $dN/d\tau$ distributions show, the resulting hydrodynamic freeze-out distribution is *not* close to the cascade distribution because one has to reproduce not only the curve given by the ridge of the wedge but *also* the exact distribution along this curve.

If the freeze-out temperature is high enough to yield a freeze-out surface with a timelike portion, we get unphysical spikes in the freeze-out distribution that are not present in the cascade calculations. This can be seen in Fig. 5 for $T_f = 200$ MeV, and in Fig. 3 for $T_f = 130$ and 200 MeV. For example, for $R_0 = 6$ fm with $T_f = 130$ MeV, Cooper-Frye frozen hydrodynamics produces most particles at around $\tau = 5.6$ fm/c. This is because the inside of the cylinder follows a 1D Bjorken evolution with $T(\tau) = T_0(\tau_0/\tau)^{1/3}$ until the rarefaction wave from the boundary arrives. The rarefaction wave travels with a speed $c_s = 1/\sqrt{3}$. If the system is large enough, most of the system reaches the freeze-out temperature *before* the rarefaction wave arrives, i.e., during the $(1+1)$D Bjorken evolution. With our parameters $T_0 = 0.5$ GeV, $T_{fo} = 130$ MeV, and $\tau_0 = 0.1$ fm/c, this gives a freeze-out for the *inside* of the cylinder at $\tau_{fo} = 5.6$ fm/c, which is in complete disagreement with our transport theory solutions. Furthermore, it does not correspond to the infinite reaction rate limit either because in that case particles freeze out very late.

Hence the peaks in $dN/d\tau$ at $\tau = 5.6$ fm/c ($T_f = 130$ MeV) and $\tau = 1.6$ fm/c ($T_f = 200$ MeV) are a clear consequence of the arbitrary freeze-out prescription using Eq. (19) with isotherm freeze-out hypersurfaces. Smearing the peaks out around their maxima does not help either because that does not change the location of the peaks, while the maximum from the cascade moves outward with increasing reaction rates.

2. Momentum space

The freeze-out distribution in momentum space is shown in Figs. 2 and 6. Figure 6 shows the freeze-out $p_\perp$-distribution for initial radii 2 fm and 6 fm, cascade cross sections 3, 15, and 60 mb compared to ideal hydrodynamics with a Cooper-Frye freeze-out at temperatures $T_f = 100$, 130, and 200 MeV. As the reaction rate increases, the small $p_\perp$ slopes rise as the system cools due to longitudinal work. The $p_\perp$ distribution seems to approach that of Cooper-Frye frozen hydrodynamics. However, this is only an illusion on a low-resolution logarithmic plot. Figure 2, where we plotted the final $p_\perp$-spectra divided by the initial $T_0 = 500$ MeV ther-
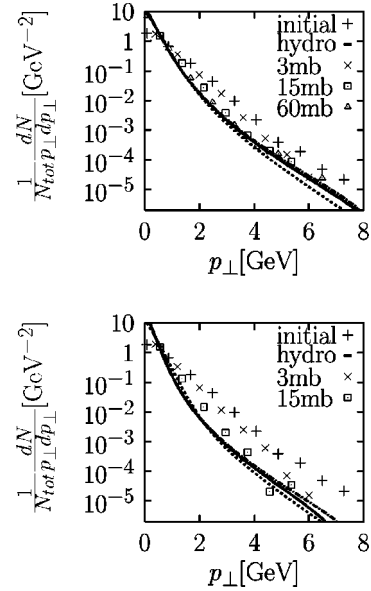

FIG. 6. The top figure shows the freeze-out $p_\perp$ distributions from an initial radius $R_0 = 2$ fm for the cascade with $\sigma = 3$, 15, 60 mb, and for ideal hydrodynamics with Cooper-Frye freeze-out with freeze-out temperatures $T_f = 100$ MeV (dashed-dotted line), 130 MeV (thick solid line), and 200 MeV (dotted line). The initial $p_\perp$ distribution is shown using pluses. The bottom figure shows the same but for an initial radius $R_0 = 6$ fm with cross sections 3 and 15 mb.

mal one, shows that there *is* a large, up to a factor of 10 difference at both low (< 0.5 GeV) and high $p_\perp$ (> 2 GeV), depending on the microscopic rates. For all the cases studied, Cooper-Frye frozen hydrodynamics has more low-$p_\perp$ particles but fewer high-$p_\perp$ ones than the cascade. This is not necessarily a general feature because the assumed hydrodynamic freeze-out temperature is an arbitrary number. A later freeze-out (lower temperature) gives a larger slope, an earlier freeze-out (higher temperature) gives a smaller one.

It is also striking that one would need rather high, $T_f \sim 300 - 450$ MeV freeze-out temperatures to get closer to the cascade $p_\perp$ spectra. We conclude that it is not possible to reproduce *both* the space-time and the momentum space transport theory freeze-out distributions using ideal hydrodynamics with the isotherm Cooper-Frye freeze-out prescription. Either one needs to treat hydrodynamic freeze-out more accurately than the Cooper-Frye prescription, or one needs to use full-scale transport theory instead of ideal hydrodynamics. The present work is a step in the latter direction, while Refs. [21–23] are important steps in the former direction looking for a simplification of the full transport theoretical problem that will still be applicable to a wide class of situations.

VI. OUTLOOK

There are many open problems in the development of covariant transport theory. The most urgent need is to develop practical convergent algorithms to incorporate inelastic

$2 \leftrightarrow 3$ processes to allow studies of chemical equilibration. Preliminary work in Ref. [13] indicated a rather slow convergence towards Lorentz covariance with particle subdivision. Unlike the $l^{-1/2}$ convergence in $2 \rightarrow 2$, a much slower $\sim l^{-1/5}$ convergence is expected in $2 \leftrightarrow 3$ processes even when nonlocal formation physics ($\Delta t > \hbar/\Delta E$) is neglected.

Also, we note that all results in this paper pertain to homogeneous initial conditions. In Ref. [30], it was shown that jets induce large nonstatistical local fluctuations that may evolve in a turbulent manner. A transport study of the evolution from such inhomogeneous initial conditions would be useful to compare to the known hydrodynamic solutions.

APPENDIX: FORMAL DEFINITION FOR FREEZE-OUT

Unlike in the cascade solution where the freeze-out distribution is trivially defined by Eq. (23), in the Boltzmann equation f changes continuously and no discrete final collisions can be identified. In this Appendix we propose a generalization of Eq. (20) which is independent of the discrete numerical cascade picture. We motivate here a *formal* definition, Eq. (26), of the freeze-out distribution using solely $f(x,\mathbf{p})$ and $W_{ij \rightarrow kl}$.

Following the notion of the "last collision," one can first compute the probability that a particle starting at a coordinate x_1^μ with momentum $\mathbf{p}_1$ does *not* collide any further. The collision rate is given by

$$\Gamma_{\text{coll}} \equiv \frac{dN_{\text{coll}}}{d^4 x}(x, \mathbf{p}_1, \mathbf{p}_2)$$
$$= f_1(x, \mathbf{p}_1) f_2(x, \mathbf{p}_2) \sigma(p_1, p_2) v_{12} d^3 p_1 d^3 p_2, \quad (A1)$$

where the relative velocity and the total cross section are given with the Lorentz scalar

$$t_{12} \equiv \sqrt{(p_1^\mu p_{2\mu})^2 - m_1^2 m_2^2} \quad (A2)$$

as

$$v_{12} = \frac{t_{12}}{E_1 E_2},$$

$$\sigma(p_1, p_2) = \frac{1}{t_{12}} \int_3 \int_4 W_{12 \rightarrow 34} \delta^4(p_1 + p_2 - p_3 - p_4).$$
$$(A3)$$

A free pointlike particle has the phase space distribution

$$f_1(x,p) = \int_0^\infty d\tau \delta^4(x - x_1 - u_1 \tau) \delta^4(p - p_1), \quad (A4)$$

where for an on-shell particle

$$\delta(p^0 - \sqrt{\mathbf{p}^2 + m^2}) = \delta(p^2 - m^2) 2\sqrt{m^2 + \mathbf{p}^2}\Theta(p_0),$$

i.e.,

$$\delta^4(p - p_1) = \delta^3(\mathbf{p} - \mathbf{p}_1)\delta(p^2 - m^2)2\sqrt{m^2 + \mathbf{p}_1^2}\Theta(p_0)$$

and thus[5]

$$f_1(x,\mathbf{p}) = \int_0^\infty d\tau \delta^4(x - x_1 - u_1 \tau)\delta^3(\mathbf{p} - \mathbf{p}_1)\frac{\sqrt{m^2 + \mathbf{p}_1^2}}{m}.$$
$$(A6)$$

Plugging this result into Eq. (A1), the probability that a free particle will not have any further collisions is[6]

$$P_0(x_1, \mathbf{p}_1) = \exp\left(-\int \Gamma_{\text{coll}} d^3 p_1 d^3 p_2 d^4 x\right)$$
$$= \exp\left(-\int \frac{d\tau d^3 p_2}{E_2 m} f_2(x_1 + u_1 \tau, \mathbf{p}_2)\right.$$
$$\left. \times \sigma(p_1, p_2) t_{12}\right). \quad (A7)$$

Now we can write the freeze-out distribution as the number of particles having a collision at x^μ with *outgoing* momentum $\mathbf{p}_1$ times the probability that these particles do not collide any further, i.e.,

$$E_1 \frac{dF_{fo}^{coll}(x, \mathbf{p}_1)}{d^4 x d^3 p_1} \equiv P_0(x, \mathbf{p}_1) \int_3 \int_4 \int_5 W_{34 \rightarrow 15}\delta^4(p_3 + p_4 - p_1$$
$$- p_5) f_3 f_4. \quad (A8)$$

This definition does not include those particles that are formed but suffer no collisions afterward. Their contribution is

$$E_1 \frac{dF_{fo}^{\text{form}}(x, \mathbf{p}_1)}{d^4 x d^3 p_1} \equiv S(x, \mathbf{p}_1) P_0(x, \mathbf{p}_1). \quad (A9)$$

Hence the final freeze-out distribution is given by Eq. (26).

---

[5]Recall, the on-shell phase space distribution is defined via

$$f(x,p) \equiv 2m\delta(p^2 - m^2)\Theta(p_0)f(x, \mathbf{p}). \quad (A5)$$

[6]This can be derived assuming that subsequent collisions are uncorrelated (just like the similar formula for the inhomogeneous Poisson distribution).

The definition (26) should be regarded as only one measure of the freeze-out distribution because it has several shortcomings. The probabilities summed are not probabilities for disjoint events. One should *exclude* the volume in space time given by all the linear paths of the already frozen-out particles. This requires knowledge of multiparticle correlations beyond the scope of the Boltzmann equation. As long as those excluded volume effects are small, Eq. (26) is adequate. A clear problem with the present formal definition is that particle number and momentum are not conserved by it as is automatic in Eq. (23). It is interesting to contrast on the other hand, the trivial way that the cascade solves this problem through Eq. (23). In cascade, the *N*-body correlations are automatically calculated and freeze-out is easily defined conserving number and total four-momentum. The continuum limit is thus subtle. Our numerical results define that continuum limit as the limit of infinite subdivisions using the cascade technique.

[1] S. R. de. Groot, *Relativistic Kinetic Theory: Principles and Applications* (North-Holland, Amsterdam, 1980), p. 1.
[2] Y. Pang, RHIC 96 Summer Study, CU-TP-815 report (unpublished); Generic Cascade Program (GCP) documentation available at WWW site http://rhic.phys.columbia.edu/rhic/gcp.
[3] B. Zhang, Comput. Phys. Commun. **109**, 193 (1998).
[4] D. Molnár, MPC 0.1.2. This parton cascade code used in the present study can be downloaded from WWW at http://www-cunuke.phys.columbia.edu/people/molnard.
[5] Proceedings of Open Standards for Cascade Models for RHIC (OSCAR), BNL-64912, 1997, edited by Miklos Gyulassy and Y. Pang; source codes and documentation for transport models under the OSCAR standard can be downloaded from the OSCAR WWW site http://www-cunuke.phys.columbia.edu/OSCAR/.
[6] M. Bleicher, E. Zabrodin, C. Spieles, S. A. Bass, C. Ernst, S. Soff, L. Bravina, M. Belkacem, H. Weber, H. Stöcker, and W. Greiner, J. Phys. G **25**, 1859 (1999).
[7] L. D. Landau, Izv. Akad. Nauk SSSR, Ser. Fiz. **17**, 51 (1953).
[8] L. P. Csernai, *Introduction to Relativistic Heavy Ion Collisions* (Wiley, New York, 1994), p. 1.
[9] *Proceedings of the International Workshop on Applicability of Relativistic Hydrodynamic Models in Heavy Ion Physics*, edited by L. P. Csernai [Heavy Ion Phys. **5**, 321 (1997)].
[10] T. S. Olson and W. A. Hiscock, Phys. Rev. D **41**, 3687 (1990).
[11] M. Gyulassy, Y. Pang, and B. Zhang, Nucl. Phys. **A626**, 999 (1997).
[12] B. Zhang, M. Gyulassy, and Y. Pang, Phys. Rev. C **58**, 1175 (1998).
[13] S. A. Bass *et al.*, Nucl. Phys. **A661**, 205 (1999).
[14] D. H. Rischke, S. Bernard, and J. A. Maruhn, Nucl. Phys. **A595**, 346 (1995); A. Dumitru and D. H. Rischke, Phys. Rev. C **59**, 354 (1999).
[15] B. Zhang, C. M. Ko, B. Li, and Z. Lin, Phys. Rev. C **61**, 067901 (2000).
[16] M. Gyulassy and X. Wang, Comput. Phys. Commun. **83**, 307 (1994).
[17] K. J. Eskola, K. Kajantie, P. V. Ruuskanen, and K. Tuominen, Nucl. Phys. **B570**, 379 (2000).
[18] F. Cooper and G. Frye, Phys. Rev. D **10**, 186 (1974).
[19] L. P. Csernai, Z. Lázár, and D. Molnár, Heavy Ion Phys. **5**, 467 (1997).
[20] K. A. Bugaev, Nucl. Phys. **A606**, 559 (1996).
[21] Cs. Anderlik, L. P. Csernai, F. Grassi, W. Greiner, Y. Hama, T. Kodama, Zs. I. Lázár, V. Magas, and H. Stöcker, Phys. Rev. C **59**, 3309 (1999).
[22] V. K. Magas, C. Anderlik, L. P. Csernai, F. Grassi, W. Greiner, Y. Hama, T. Kodama, Zs. I. Lázár, and H. Stöcker, Phys. Lett. B **459**, 33 (1999); Nucl. Phys. **A661**, 596 (1999); Heavy Ion Phys. **9**, 193 (1999).
[23] Cs. Anderlik, Zs. I. Lázár, V. K. Magas, L. P. Csernai, H. Stöcker, and W. Greiner, Phys. Rev. C **59**, 388 (1999).
[24] F. Grassi, Y. Hama, and T. Kodama, Z. Phys. C **73**, 153 (1996); Phys. Lett. B **355**, 9 (1995).
[25] S. Gavin, M. Gyulassy, and A. Jackson, Phys. Lett. B **207**, 257 (1988).
[26] S. A. Bass, A. Dumitru, M. Bleicher, L. Bravina, E. Zabrodin, H. Stöcker, and W. Greiner, Phys. Rev. C **60**, 021902 (1999).
[27] S. A. Bass and A. Dumitru, Phys. Rev. C **61**, 064909 (2000).
[28] S. S. Padula, M. Gyulassy, and S. Gavin, Nucl. Phys. **B329**, 357 (1990).
[29] J. D. Bjorken, Phys. Rev. D **27**, 140 (1983).
[30] M. Gyulassy, D. Rischke, and B. Zhang, Nucl. Phys. **A613**, 397 (1997).